Robotica (2017) volume 35, pp. 636–653.
doi:10.1017/S0263574715000740

Analysis of sliding behavior of a biped robot in centroid acceleration space

Taku Senoo* and Masatoshi Ishikawa

Department of Information Physics and Computing, Graduate School of Information Science and Technology, University of Tokyo, 7-3-1 Hongo, Bunkyo-ku, Tokyo 113-8656, Japan

(Accepted August 7, 2015. First published online: September 4, 2015)

SUMMARY

In this article, a two-dimensional analysis of biped robot sliding dynamics is performed. First, the dynamics of a biped robot based on feet-slip are derived using the coulomb friction model. The state transition can be formulated in the centroid acceleration space whose diagram is defined as a "triangle of sliding friction" (TSF). The TSF's characteristics are explained by focusing on comparison with the cone of friction which has a similar state decision diagram. Next, for the behavioral simulation of a concrete model, a 2-DOF biped robot is used to analyze the sliding features in terms of the asymmetry of the dynamics of each leg. Finally, the sliding characteristics are applied to the two tasks of running and somersaulting. The results show the robot takes short rapid repetitive steps for running based on frictional asymmetry and theoretically based on torque asymmetry can make one revolution using the large angular momentum acquired during sliding motion.

KEYWORDS: Biped robot; Sliding; State transition; Running; Somersault.

1. Introduction

Biped robots have a high degree of physical and psychological compatibility with human society. This promotes ambitious research and anticipation of deployment to real society. For biped robots, the contact state between the leg and the ground is important because it determines stability and mobility since the absolute position and altitude are controlled through the ground reaction force. The contact state, which is attributable to friction, is classified roughly into two groups: stationary without relative displacement and sliding with relative displacement. As typified by the walking motion, the stationary state is commonly assumed with legged locomotion. However, there are some cases where sliding is efficiently harnessed such as translational slip including skating,[1,2] skiing,[3–5] and rotational slip including a turn[6–9] not based on stepping motions. In addition, an error recovery function is needed for dealing with unpredictable slips, further demonstrating the importance of analysis on legged sliding motion.

In fact, translational sliding of biped robots appears under a variety of circumstances. Kaneko *et al.* used a slip observer to detect the slip of an HRP-2 walking on the ground with low friction and stabilized the robot not to fall down by controlling the body axis.[10] Higashimori *et al.* designed a two-legged robot using a small actuator with a high torque-weight ratio and achieved a high jump motion based on slips of both legs in the inner direction.[11] Nemec *et al.* achieved control and navigation of a 3-DOF skiing robot that is capable of autonomous skiing on a ski slope based on recognition using visual feedback.[3] These experiments addressed sliding generally not by analysis of the sliding itself nor by reflecting the features of sliding dynamics, but by common predictive control or sensory feedback compensation. In contrast, robots in the shape of a snake offer valuable insights for the gliding principle.[12,13] However, it is difficult to apply gliding principles directly to biped robots because the basis for gliding is formed by a continuous structure contacting the ground along the body axis or a discrete set of multiple friction contact points to achieve undulatory locomotion.

* Corresponding author. E-mail: Taku_Seno@ipc.i.u-tokyo.ac.jp

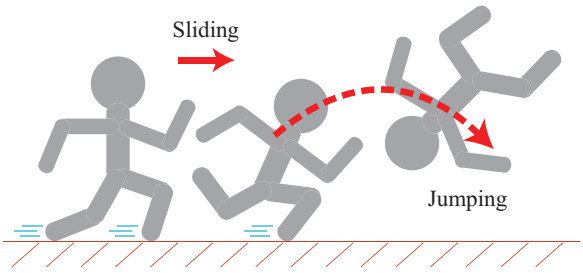

Fig. 1 Concept of biped sliding motion.

As for biped locomotion incorporating frictional analysis, walking with stick-slip transitions has been undertaken.[14,15] Stick-slip transitions are effective for dynamic locomotion but cannot deal with the state transition from slip to a non-contact phase such as when one leg comes off the floor and the robot almost falls over while sliding because they are based on a cone of friction regarding the contact phase. Today, there is insufficient knowledge of the sliding characteristics of biped robots.

This article reports on analysis of the sliding movement of a biped robot based on the coulomb friction model and verifies examples of legged motion using sliding motion. Our objective is to systematize the state transitions of biped robots focusing on sliding behavior for simple state decisions and to derive sliding characteristics from the analysis for sliding control predicated on the fact that sliding information is difficult to accurately and directly detect with sensors and may be more useful when obtained from dynamics analysis in advance of the initiation of sliding. First, the mechanical model of a biped robot is explained in the sagittal plane. The state transition between sliding and takeoff shown in Fig. 1 is formulated in centroid acceleration space. The characteristics of the formulated diagram are also derived by comparison with a similar cone of friction to determine the state transition between the stationary and sliding phases. Next, concrete sliding behavior is simulated using a 2-DOF model. In particular, the effects of the coefficients of sliding friction and input torque are discussed. Finally, the application of the sliding features from analysis to running and somersaulting are proposed. These results demonstrate the validity of the analysis of sliding dynamics.

2. Sliding Dynamics of a Biped Robot

In this section, modeling is based on the assumption that translational sliding is caused without considering the state with feet fixed to the ground. We consider the states including two-legs sliding, one-leg sliding, and jumping and derive the condition when each leg leaves the ground in order to formulate the state transition.

2.1. Mechanical model[16]

Consider a biped robot model that consists of a trunk segment and two legs. Each leg ($i = 1, 2$) consists of n_i links, and each link is driven independently by a rotational motor. To simplify analyses, a two-dimensional model is used. Assume that the biped robot consists of a rigid body, and each leg contacts the ground at one point. The x-axis is set along the horizontal ground, and the z-axis is the vertical direction in the standard coordinate system shown in Fig. 2(a). When only the feet contact the ground, the equations of translational motion are derived as follows:

$$m_0 \ddot{\boldsymbol{r}}_{c0} = m_0 \boldsymbol{g} - \sum_i {}^1\boldsymbol{F}_i, \qquad {}^j m_i \, {}^j\ddot{\boldsymbol{r}}_{ci} = {}^j m_i \, \boldsymbol{g} + {}^j\boldsymbol{F}_i - {}^{j+1}\boldsymbol{F}_i, \qquad \text{where } {}^{n_i+1}\boldsymbol{F}_i \equiv -\boldsymbol{N}_i. \quad (1)$$

Here ${}^j m_i$ is the mass, ${}^j\boldsymbol{r}_{ci}$ represents the center of gravity with respect to each link, $\boldsymbol{g} = [0, -g]^T$ is gravity acceleration, ${}^j\boldsymbol{F}_i$ is the internal force, and $\boldsymbol{N}_i$ is the ground reaction force. An index of 0 means the value of the trunk, and indexes to the upper left j and lower right i of a variable mean the jth link and ith leg, respectively. The forces act on the biped robot as shown in Fig. 2(b). The

https://doi.org/10.1017/S0263574715000740 Published online by Cambridge University Press

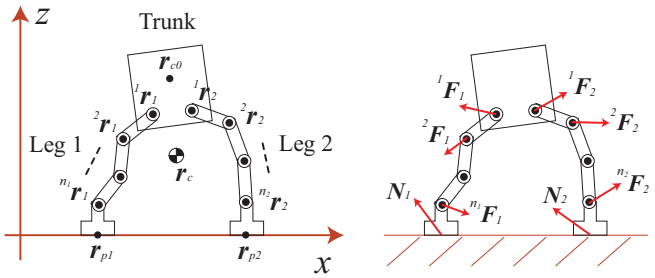

(a) Coordinate system (b) Force

Fig. 2 Mechanical model.

equations of rotational motion are derived as follows:

$$
\begin{aligned}
I_0\,\dot{\omega}_0 &= \sum_i \left\{ -{}^1\tau_i + ({}^1\boldsymbol{r}_i - \boldsymbol{r}_{c0}) \times (-{}^1\boldsymbol{F}_i) + {}^1k_i({}^1\omega_i - \omega_0) \right\}, \\
{}^jI_i\,{}^j\dot{\omega}_i &= ({}^j\boldsymbol{r}_i - {}^j\boldsymbol{r}_{ci}) \times {}^j\boldsymbol{F}_i + ({}^{j+1}\boldsymbol{r}_i - {}^j\boldsymbol{r}_{ci}) \times (-{}^{j+1}\boldsymbol{F}_i) - {}^jk_i\,({}^j\omega_i - {}^{j-1}\omega_i) \\
&\quad + {}^{j+1}k_i\,({}^{j+1}\omega_i - {}^j\omega_i) + {}^j\tau_i - {}^{j+1}\tau_i, \\
&\quad \text{where } {}^{n_i+1}\boldsymbol{r}_i \equiv \boldsymbol{r}_{pi},\ {}^{n_i+1}\tau_i \equiv 0,\ {}^{n_i+1}k_i \equiv 0,\ {}^{n_i+1}\omega_i \equiv 0,\ {}^0\omega_i \equiv \omega_0.
\end{aligned}
\tag{2}
$$

Here ${}^jI_i$ is the moment of inertia about the center of gravity, ${}^j\omega_i$ is the angular velocity, ${}^j\tau_i$ is the torque, ${}^j\boldsymbol{r}_i$ is the joint position, $\boldsymbol{r}_{pi}$ is the contact position between the leg and the ground, ${}^jk_i$ is the coefficient of viscous friction of the motor, the cross product is redefined as $\boldsymbol{a} \times \boldsymbol{b} \equiv a_x b_z - a_z b_x$, and the + sign of the variable is defined as a counter-clockwise rotation.

In this article, coulomb friction is considered to be a sliding model where the sliding frictional force is directly proportional to the normal force. In this case, the ground reaction force is decomposed into normal force and sliding friction as follows:

$$
\boldsymbol{N}_i = N_{iz} \begin{bmatrix} \pm\mu_i \\ 1 \end{bmatrix} \equiv N_{iz}\boldsymbol{\mu}_i, \tag{3}
$$

where μ_i is the coefficient of sliding friction between the feet and the ground, and $\boldsymbol{\mu}_i$ is defined as the friction vector including the direction of sliding. Sliding frictional forces act in the opposite direction of sliding, and the friction vectors of both legs with same coefficients of sliding friction are different if both legs slide in opposite directions. Note that the static ground reaction force cannot be described as Eq. (3) even if the coefficient of sliding friction is replaced with that of static friction. This is because static friction generates necessary and sufficient frictional force to keep the feet fixed without sliding, and only the maximum value is proportional to the normal force. That is, static friction does not normally generate a frictional force proportional to the normal force whereas sliding friction always generates such force.

The following relational expression is derived from the sum of all equations of Eq. (1) as:

$$
m_s\ddot{\boldsymbol{r}}_c = m_s\boldsymbol{g} + \sum_i \boldsymbol{N}_i, \quad \text{where } m_s \equiv m_0 + \sum_{i,\,j} {}^jm_i, \quad \boldsymbol{r}_c \equiv m_s^{-1}\left(m_0\boldsymbol{r}_{c0} + \sum_{i,\,j} {}^jm_i\,{}^j\boldsymbol{r}_{ci} \right). \tag{4}
$$

Here m_s is the total mass of the robot, and $\boldsymbol{r}_c$ is the position of the total center of gravity. As for rotational motion, the temporal differentiation of the angular momentum is calculated as

$$
\dot{L}_G = \sum_i \left\{ (\boldsymbol{r}_{pi} - \boldsymbol{r}_c) \times \boldsymbol{N}_i \right\}. \tag{5}
$$

https://doi.org/10.1017/S0263574715000740 Published online by Cambridge University Press

Next, consider the three states as shown in Fig. 1: two-legs sliding, one-leg sliding, and jumping. Then the concrete forms of Eqs. (4) and (5) vary according to the state, and they are derived below.

2.1.1. Two-legs sliding. When sliding friction vectors are different as $\boldsymbol{\mu}_1 \neq \boldsymbol{\mu}_2$, the normal force is calculated using the centroid motion by Eqs. (3) and (4) as

$$N_{1z} = \frac{m_s(\ddot{\boldsymbol{r}}_c - \boldsymbol{g}) \times \boldsymbol{\mu}_2}{\boldsymbol{\mu}_1 \times \boldsymbol{\mu}_2}, \quad N_{2z} = \frac{m_s(\ddot{\boldsymbol{r}}_c - \boldsymbol{g}) \times \boldsymbol{\mu}_1}{\boldsymbol{\mu}_2 \times \boldsymbol{\mu}_1}. \tag{6}$$

On the other hand, the normal force cannot be described by Eq. (6) due to the dimensionality reduction of equations when $\boldsymbol{\mu}_1 = \boldsymbol{\mu}_2$. Therefore, we assume $\boldsymbol{\mu}_1 \neq \boldsymbol{\mu}_2$ in what follows. Then the following relation about the angular momentum is satisfied by Eq. (5):

$$\dot{L}_G = \frac{m_s(\ddot{\boldsymbol{r}}_c - \boldsymbol{g}) \times \boldsymbol{\gamma}}{\boldsymbol{\mu}_1 \times \boldsymbol{\mu}_2}, \quad \text{where } \boldsymbol{\gamma} \equiv \left\{(\boldsymbol{r}_{p1} - \boldsymbol{r}_c) \times \boldsymbol{\mu}_1\right\}\boldsymbol{\mu}_2 - \left\{(\boldsymbol{r}_{p2} - \boldsymbol{r}_c) \times \boldsymbol{\mu}_2\right\}\boldsymbol{\mu}_1 \tag{7}$$

2.1.2. One-leg sliding. When one leg slides on the ground and the other leg is off the ground, the centroid motion and the normal force are obtained as the state with no ground reaction concerning the swing leg from Eqs. (3) and (4):

$$\begin{cases} (\ddot{\boldsymbol{r}}_c - \boldsymbol{g}) \times \boldsymbol{\mu}_2 = 0, & N_{2z} = m_s(\ddot{r}_{cz} + g) \quad \text{if } \boldsymbol{N}_1 = \boldsymbol{0} \\ (\ddot{\boldsymbol{r}}_c - \boldsymbol{g}) \times \boldsymbol{\mu}_1 = 0, & N_{1z} = m_s(\ddot{r}_{cz} + g) \quad \text{if } \boldsymbol{N}_2 = \boldsymbol{0} \end{cases}, \tag{8}$$

In the same manner, the following relation about the angular momentum is true from Eq. (5):

$$\dot{L}_G = \begin{cases} m_s(\ddot{r}_{cz} + g)(\boldsymbol{r}_{p2} - \boldsymbol{r}_c) \times \boldsymbol{\mu}_2 & \text{if } \boldsymbol{N}_1 = \boldsymbol{0} \\ m_s(\ddot{r}_{cz} + g)(\boldsymbol{r}_{p1} - \boldsymbol{r}_c) \times \boldsymbol{\mu}_1 & \text{if } \boldsymbol{N}_2 = \boldsymbol{0} \end{cases}, \tag{9}$$

2.1.3. Jumping. When both legs are off the ground, the centroid motion is obtained as the state with no ground reaction with both legs from Eq. (4):

$$\ddot{\boldsymbol{r}}_c = \boldsymbol{g} \quad \text{if } \boldsymbol{N}_1 = \boldsymbol{N}_2 = \boldsymbol{0}. \tag{10}$$

The trajectory of the center of gravity forms a parabola after jumping because the external forces consist of only gravity in the air. In the same manner, angular momentum is conserved from Eq. (5):

$$\dot{L}_G = 0 \quad \text{if } \boldsymbol{N}_1 = \boldsymbol{N}_2 = \boldsymbol{0}. \tag{11}$$

2.2. Analysis of dynamics

2.2.1. State transition. Consider the condition of the state transition between the above three states. Because the robot starts to jump from the ground when the normal force is zero, the timing of takeoff for each leg depends on the acceleration of the centroid from Eqs. (6) and (8). In the case where Leg 1 leaves the ground before Leg 2, the condition is described as $(\ddot{\boldsymbol{r}}_c - \boldsymbol{g}) \times \boldsymbol{\mu}_2 = 0$ from Eq. (6). It turns out that this condition becomes the acceleration constraint in the sliding motion with Leg 2 from Eq. (8). Then the equation of $\ddot{\boldsymbol{r}}_c = \boldsymbol{g}$ is both the condition for takeoff of Leg 2 and the acceleration constraint in the air from Eqs. (8) and (10). That is, the condition for takeoff of each leg becomes the acceleration constraint in the next phase which means that smooth transition in the acceleration level is achieved. The characteristics are also true in the same manner if Leg 2 leaves the ground before Leg 1.

These characteristics can be organized in acceleration space as shown in Fig. 3. Because the normal force is always greater than zero, the movable range of acceleration is equivalent to the following

https://doi.org/10.1017/S0263574715000740 Published online by Cambridge University Press

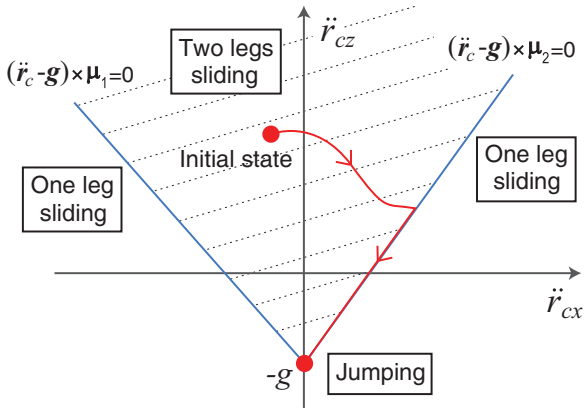

Fig. 3 State transition in acceleration space.

area bounded by the line of $(\ddot{\boldsymbol{r}}_c-\boldsymbol{g})\times\boldsymbol{\mu}_1=0$ and $(\ddot{\boldsymbol{r}}_c-\boldsymbol{g})\times\boldsymbol{\mu}_2=0$:

$$\begin{cases}(\ddot{\boldsymbol{r}}_c-\boldsymbol{g})\times\boldsymbol{\mu}_1\le 0,\ (\ddot{\boldsymbol{r}}_c-\boldsymbol{g})\times\boldsymbol{\mu}_2\ge 0 & \text{if } \boldsymbol{\mu}_1\times\boldsymbol{\mu}_2>0\\ (\ddot{\boldsymbol{r}}_c-\boldsymbol{g})\times\boldsymbol{\mu}_1\ge 0,\ (\ddot{\boldsymbol{r}}_c-\boldsymbol{g})\times\boldsymbol{\mu}_2\le 0 & \text{if } \boldsymbol{\mu}_1\times\boldsymbol{\mu}_2<0\end{cases}, \tag{12}$$

Once acceleration reaches the boundary line, the state transitions from sliding with two legs to sliding with one leg. Then the state moves along the boundary line and converges on the jumping state of $\ddot{\boldsymbol{r}}_c=\boldsymbol{g}$. From the figure, both legs start to jump at the same time without going through a single support phase only when the state does not have any contact with the boundary line until jumping and directly converges on the point of $\ddot{\boldsymbol{r}}_c=\boldsymbol{g}$.

2.2.2. Comparison with cone of friction. The state transition diagram in acceleration space shown in Fig. 3 is similar to a cone of friction which determines the state between stationary and sliding, however, it is essentially different. We define it as a "triangle of sliding friction" in contradistinction to a cone of friction and describe main differences below.

- Coordinate: A cone of friction is formulated in the force coordinate based on the contact position whereas a TSF is formulated in the acceleration coordinate relative to the centroid. In both diagrams, it is easy visually to determine the current state. In a biped robot, there are two cones of friction located on each foot whereas there is only one TSF because it is associated with the centroid.
- Domain: The acting force can exist in and out of a cone of friction whereas centroid acceleration is restricted to the inside of a TSF. This is because the static frictional force is determined essentially independently of normal force whereas the sliding frictional force specifically corresponds to the normal force at all times.
- Shape: The boundaries of a cone of friction are equivalent to the generatrix of the cone and form a symmetrical shape with respect to the normal direction to the contact point. On the other hand, because the boundaries of a TSF correspond to each leg, they form an inclined shape in the half plane as shown in Fig. 4(a) especially when both legs slide in the same direction. In 3D, a cone of friction forms a 3D cone whereas a TSF essentially has an invariant triangle shape, and the state is constrained in the 2D plane (See appendix for details).

2.2.3. Range of application. TSF can be applied to biped robots with an upper limb or a head connected to the trunk because the formulation is based on centroid movement. On the other hand, in robots with no fewer than three legs, the normal force cannot be explicitly described as a function of the centroid acceleration as in Eq. (6) because the two boundary lines of TSF correspond to two legs. However, TSF can be still applicable to multi-legged robots when the number of legs on the ground does not exceed two. Moreover, the ZMP on each foot should be set as the contact point when the contact area cannot be ignored because frictional force does not depend on the contact area in the coulomb model. In a slope with angle ϕ, TSF holds with the ϕ-rotated state as shown in Fig. 4(b)

https://doi.org/10.1017/S0263574715000740 Published online by Cambridge University Press

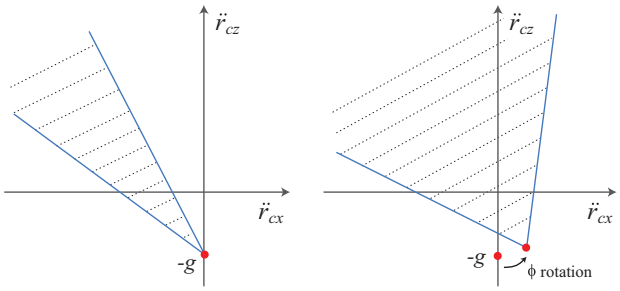

(a) Case of slip in the same direction (b) Case of a slope with angle ϕ

Fig. 4 Change in triangle of sliding friction.

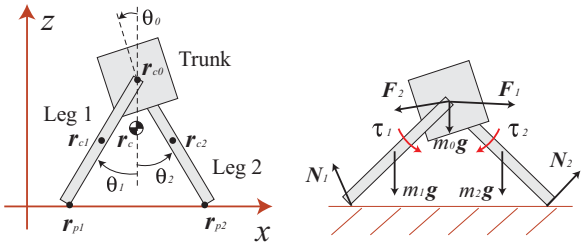

(a) Coordinate system (b) Force and torque

Fig. 5 2-DOF model showing the connection of each leg to the trunk centroid.

by setting the x-axis as the slope direction; the z-axis is perpendicular, and gravity is redefined as $\boldsymbol{g} = [g \sin\phi, -g \cos\phi]^T$.

2.3. Discussion on acceleration and deceleration

Considering that the frictional force acts in the reverse direction of sliding, when both legs slide in the same direction, the centroid motion inevitably decelerates because the net frictional force opposes sliding as seen in Eq. (4). This corresponds to the existence of TSF in left half plane as shown in Fig. 4(a). On the other hand, in three-dimensional sliding, a pushing force can be generated in a direction perpendicular to the sliding direction which corresponds to the y-axis in the model. This enables accelerated motion by using the traveling component of the pushing force, for example, which is achieved by forming a V-shaped opening to the ice surface in ice skating.[17,18] That is, in the 2D coulomb friction model, the horizontal movement is driven only by the sliding frictional force because a pushing force cannot be generated. Hence, the net internal forces are counterbalanced with respect to the centroid motion meaning that the centroid cannot be accelerated in the traveling direction when both legs slide in the same direction. In contrast, when both legs slide opposite to each other, the centroid motion can be accelerated even in the 2D case using different sliding frictional forces in each foot.

3. Motion Analysis of a 2-Dof MODEL

In this section, the behavior of a concrete 2-DOF mechanical model is analyzed. In particular, the oppositely-directed two-legs sliding motion can be controlled to accelerate without external force to simulate the effect of friction and torque on sliding behavior.

3.1. 2-DOF model

To clarify the effect of each parameter on the robot behavior, consider the following case where each leg consists of a 1-DOF straight link, and both legs are connected to the trunk centroid as shown in Fig. 5:

$$n_1 = n_2 = 1, \ {}^1\boldsymbol{r}_1 = {}^1\boldsymbol{r}_2 = \boldsymbol{r}_{c0}. \tag{13}$$

https://doi.org/10.1017/S0263574715000740 Published online by Cambridge University Press

The upper left index is omitted to simplify the description in what follows because each leg has only one link. In addition, assume that both legs have the following symmetrical kinematics and dynamics parameters:

$$m_1 = m_2 \equiv m,\ l_1 = l_2 \equiv l,\ l_{g1} = l_{g2} \equiv l_g,\ I_1 = I_2 \equiv I,\ k_1 = k_2 \equiv k, \tag{14}$$

where l_i is the length of each leg, and l_{gi} is the length from the joint position to the centroid of each leg. Define θ_i as the rotational angle set to the upright posture at zero radians. Then, the following geometric constraint is true

$$\theta_1 = -\theta_2 \equiv \theta. \tag{15}$$

The centroid of each leg $\boldsymbol{r}_{ci}$ $(i = 1, 2)$ is represented as

$$\boldsymbol{r}_{ci} = l_g \begin{bmatrix} S_{\theta_i} \\ -C_{\theta_i} \end{bmatrix} + \boldsymbol{r}_{c0} = (l - l_g) \begin{bmatrix} -S_{\theta_i} \\ C_{\theta_i} \end{bmatrix} + \boldsymbol{r}_{pi}, \tag{16}$$

where $S_\theta \equiv \sin\theta$ and $C_\theta \equiv \cos\theta$.

In the case of movement of both legs in the inner direction, the friction vector is expressed as

$$\boldsymbol{\mu}_1 = \begin{bmatrix} -\mu_1 \\ 1 \end{bmatrix}, \quad \boldsymbol{\mu}_2 = \begin{bmatrix} \mu_2 \\ 1 \end{bmatrix}. \tag{17}$$

Then, the following relation about the acceleration is true by substituting Eqs. (1) and (6) in Eq. (2) and eliminating the internal and the ground reaction forces:

$$m_s(\ddot{\boldsymbol{r}}_c - \boldsymbol{g}) \times \boldsymbol{\gamma} = -(\boldsymbol{\mu}_1 \times \boldsymbol{\mu}_2)(\tau_1 + \tau_2), \quad \text{where } \boldsymbol{\gamma} = l \begin{bmatrix} (\mu_2 - \mu_1)S_\theta \\ 2S_\theta - (\mu_1 + \mu_2)\left(1 - \frac{2ml_g}{m_s l}\right)C_\theta \end{bmatrix}. \tag{18}$$

Temporal differentiation of angular momentum depends only on the input torque from Eqs. (7) and (18):

$$\dot{L}_G = -(\tau_1 + \tau_2). \tag{19}$$

The angular momentum of the trunk represents the total value because both legs are counterbalanced by geometric symmetry. The rotational motion of the trunk is expressed by Eqs. (2) and (13) as

$$I_0\dot{\omega}_0 + 2k\omega_0 + \tau_1 + \tau_2 = 0. \tag{20}$$

The state path in the acceleration space makes a curve expressed by Eq. (18). It proves that the acceleration $\ddot{\boldsymbol{r}}_c$ is determined not by the angular velocity $\dot{\theta}$ but by the altitude θ. The intersection $\boldsymbol{\eta}_i$ of the state path with the boundary $(\ddot{\boldsymbol{r}}_c - \boldsymbol{g}) \times \boldsymbol{\mu}_i = 0$ is calculated as

$$\boldsymbol{\eta}_i = -\frac{(\boldsymbol{\mu}_1 \times \boldsymbol{\mu}_2)}{m_s(\boldsymbol{\mu}_i \times \boldsymbol{\gamma})}(\tau_1 + \tau_2)\boldsymbol{\mu}_i + \boldsymbol{g}. \tag{21}$$

The intersection corresponds to the state transition into one-leg sliding.

3.2. Numerical simulation

Let us confirm the effects of the coefficients of sliding friction and input torque which greatly affect robotic behavior. Sliding movement was simulated on the condition that both legs were initially opened with initial velocity of 0, and constant torque was applied until both legs left the ground. With both parameters symmetrical on both legs, only vertical motion is generated as shown in Fig. 6(a). The cases with asymmetric parameters are analyzed as follows. The parameters were determined with reference to the experimental setting[19] shown in Table I.

https://doi.org/10.1017/S0263574715000740 Published online by Cambridge University Press

Table I. Simulation parameters.

l [m]	l_g [m]	m [kg]	m_0 [kg]	I [kgm^2]	k [Ns]	g [m/s^2]
0.1	0.05	0.05	0.2	4.17×10^{-5}	0.0568	9.8

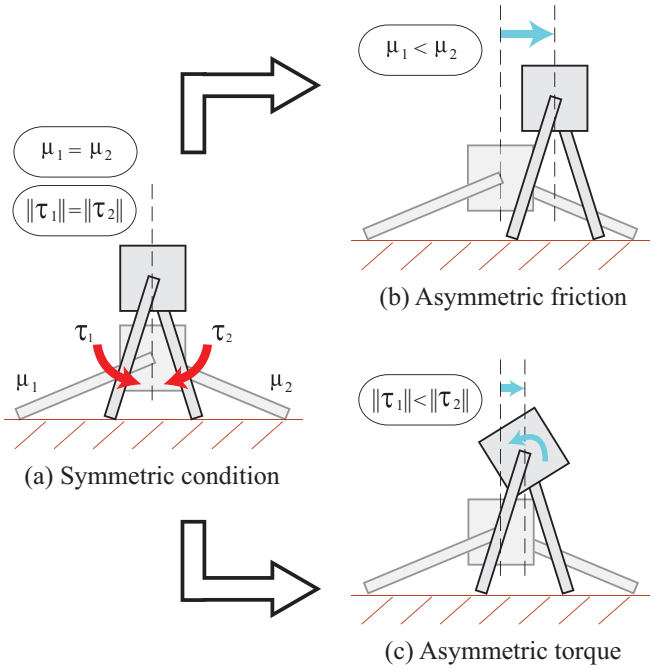

Fig. 6 Sliding movement of horizontal translation and trunk rotation.

3.2.1. Case of asymmetric coefficients of sliding friction. Consider the case where both legs are set to have symmetric input torque and asymmetric coefficients of sliding friction:

$$\tau_1 = -\tau_2 \equiv \tau, \quad \mu_1 \neq \mu_2. \tag{22}$$

Figure 7 shows the results when setting the torque $\tau = 0.7$ Nm and coefficients of sliding friction to $\mu_1 = 0.4$, $\mu_2 = 0.6$. In Fig. 7(a), the normal force of the leg with the lower friction coefficient is greater than that of the other leg until both legs leave the ground. This is attributable to the generation of asymmetrical internal forces because of the different friction coefficients on both legs. As for the timing of takeoff, the normal forces of both legs simultaneously reach 0 at $t = 0.087$ s. That is, the symmetry of torque for both legs results in the simultaneous timing of takeoff regardless of asymmetry of sliding frictions.

The time response of the angular velocity is shown in Fig. 7(b). While the angular velocities of both legs increase, the trunk does not rotate. This corresponds to the fact that the solution of Eq. (20) is expressed as $\omega_0(t) = 0$ with the initial condition of $\omega_0(0) = 0$. Moreover, this also corresponds to the fact that the angular momentum is always kept at zero with an initial value of zero because $\dot{L}_G(t) = 0$ is satisfied from Eqs. (19) and (22). The results prove that the asymmetry in the coefficients of sliding friction do not contribute to rotational motion.

The time response of the horizontal velocity is shown in Fig. 7(c). It turns out that the robot accelerates towards the leg with the higher friction until takeoff. Figure 7(d) shows the TSF and the state path. The state directly converges on the jumping point from the initial state. This corresponds to the fact that the state path intersects the boundary only at the jumping point, and both legs simultaneously start to leave the ground without going through a single support phase as $\boldsymbol{\eta}_i = \boldsymbol{g}$ is true from Eqs. (21) and (22). The frame format of the sliding motion is shown in Fig. 6(b).

https://doi.org/10.1017/S0263574715000740 Published online by Cambridge University Press

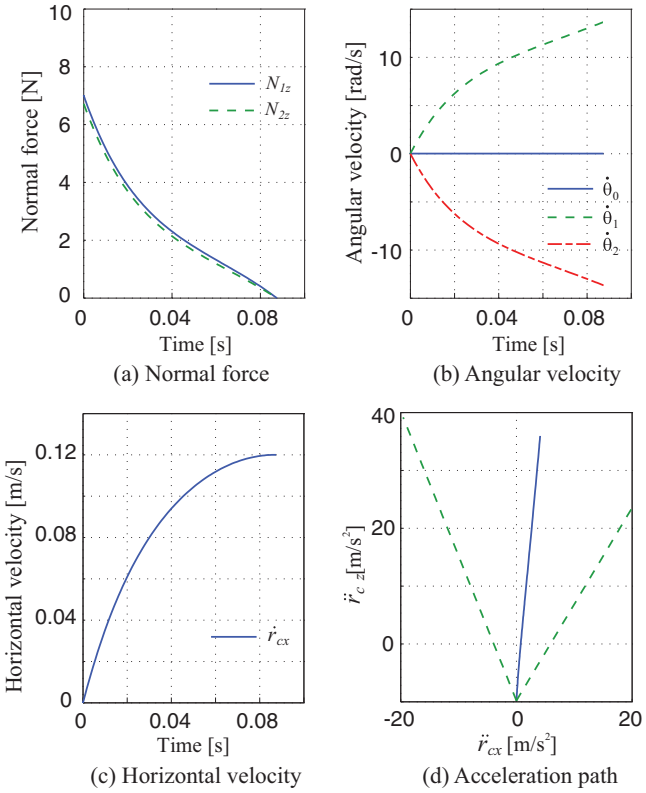

Fig. 7 Simulation results with asymmetric friction.

3.2.2. Case of asymmetric input torque. Consider the case where both legs are set to have asymmetric input torque and symmetric coefficients of sliding friction:

$$\tau_1 \neq -\tau_2, \quad \mu_1 = \mu_2 \equiv \mu. \tag{23}$$

Figure 8 shows the results when setting the torque $\tau_1 = 0.45$ Nm, $\tau_2 = -0.9$ Nm and coefficients of sliding friction as $\mu = 0.5$. From Fig. 8(a), the normal forces vary greatly between both legs just after the start time, however, they quickly converge to the same value, and this behavior continues until takeoff. This is attributable to reaching equilibrium with respect to the forces acting on both legs because of the energy dissipation by the viscous friction of motors. Because the normal force of the leg with lower torque is always slightly lower than that of the other leg, the leg with the lower torque leaves the ground first, and the other leg follows after 4 microseconds.

The time response of the angular velocity is shown in Fig. 8(b). It turns out that the angular velocity of the trunk converges to the constant value just after the start time. This corresponds to the fact that the solution of Eq. (20) is expressed as $\omega_0(t) = -\frac{\tau_1+\tau_2}{2k}\{1-\exp(-\frac{2k}{I_0}t)\}$. Considering the exponential change in angular velocity, the convergence time of the angular velocity of the trunk is quite short compared with that of both legs because the viscous friction of the two motors acts on the trunk.

The time response of the horizontal velocity is shown in Fig. 8(c). The sliding motion is generated towards the leg with the higher torque, however, the velocity quickly converges and maintains a constant value. Actually, the sliding distance is quite short, about 5 mm. Figure 8(d) shows the TSF and the state path. The state heads towards the line of $\ddot{r}_{cx} = 0$ from the initial state and then moves along the line. Strictly speaking, because the angular velocity cannot converge to a constant value in finite time, the state path intersects with the boundary near the jumping point once, then the state with one-leg sliding appears. The frame format of sliding motion is shown in Fig. 6(c).

3.3. Discussion

In terms of horizontal movement based on sliding, the robot accelerates towards the leg with higher friction or higher torque, however, there is a large difference between the two. With asymmetry

https://doi.org/10.1017/S0263574715000740 Published online by Cambridge University Press

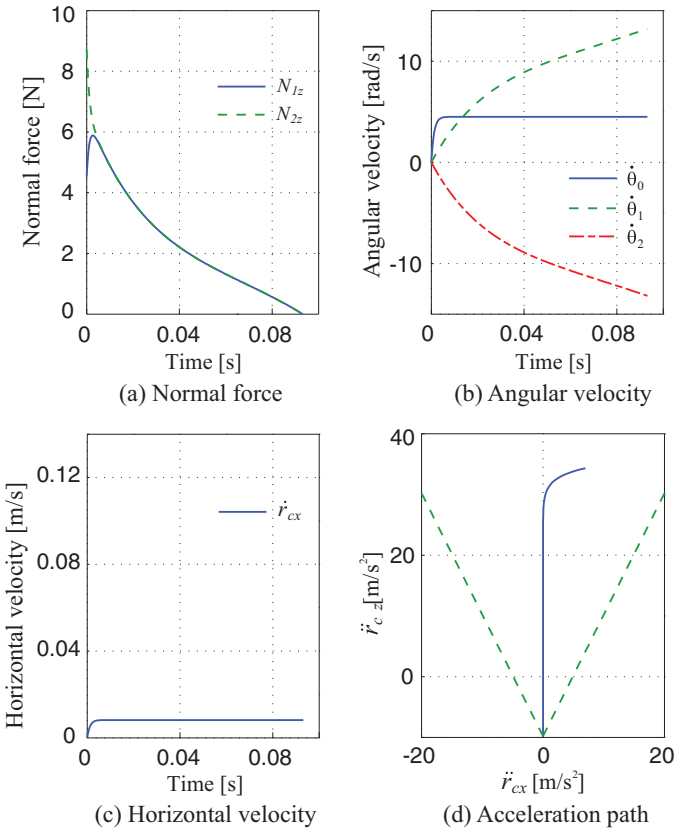

Fig. 8 Simulation results with asymmetric torque.

of the coefficients of sliding friction, the velocity continues to increase while sliding because the acceleration gradually decreases and reaches 0 at takeoff. On the other hand, with asymmetry of input torques, the robot transitions to the jumping state with very low velocity because the acceleration converges to 0 just after the start time. Accordingly, for achieving horizontal movement based on sliding, asymmetry of the coefficients of sliding friction is more effective than asymmetry of input torques.

Rotational motion is affected not by the coefficients of sliding friction but greatly by the asymmetry of input torques. In fact, as the asymmetry in torques gets larger, the angular momentum increases from Eq. (19), and the angular velocity of the trunk $\omega_0(\infty) = -\frac{\tau_1+\tau_2}{2k}$ also increases. In addition, with symmetric torques, the rotational speed exponentially decreases to 0 from Eq. (20) even when the initial angular velocity is not 0. Accordingly, when viewed from the energy perspective, the larger the asymmetry of input torques, the larger the conversion efficiency to rotational kinetic energy is.

The reaction torque from both legs act on the trunk. They are counterbalanced in the case of symmetric torque whereas the difference generates rotational motion in the case of asymmetric torques. From Fig. 9(a), which shows the results with asymmetric coefficients of sliding friction and asymmetric torque, the rotational motion converges on the state corresponding to symmetric torque expressed in Eq. (22) because of the viscous friction of the motors. In addition, as the viscous friction gets lower, the state with one-leg sliding which moves along the boundary definitely appears, and the convergence velocity decreases (Fig. 9(b) which shows the results with varying viscous frictions on the conditions of Eq. (23)). As a result, the viscous friction of the motors has the effect of generating rotational motion of the trunk so that it compensates for the energy difference caused by reducing the torque asymmetry and converging to the state corresponding to symmetric torque. Even assuming that there is no viscous friction, actual motors have a limit of rotational velocity due to electrical equilibrium, so energy dissipation also occurs.

The time response of the x position regarding the ZMP r_{zmp}, the ground point r_{pix}, and the trunk r_{c0x} is shown in Fig. 10 under the same conditions as Figs. 7 and 8. Note that r_{c0x} also corresponds

https://doi.org/10.1017/S0263574715000740 Published online by Cambridge University Press

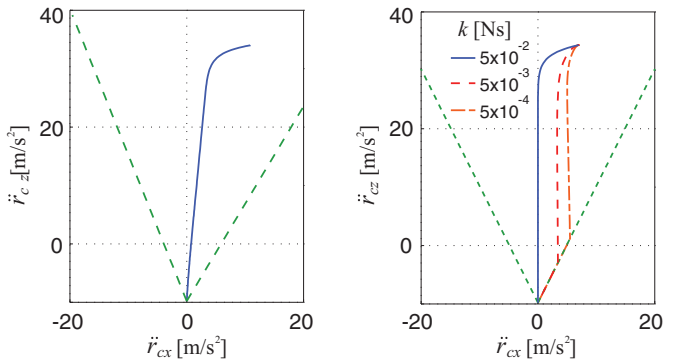

(a) Both parameters asymmetric (b) Change of viscous friction

Fig. 9 Change of state path in a triangle of sliding friction.

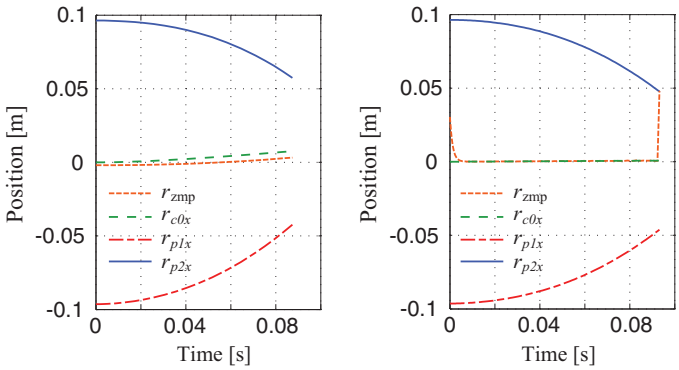

(a) Asymmetric friction (b) Asymmetric torque

Fig. 10 ZMP trajectory during sliding motion.

to the center of the support polygon during the double support phase in the model. In the case of asymmetric friction, the ZMP exists near the center of the support polygon without moving toward the ground point until takeoff. This means that both legs simultaneously leave the ground because ZMP is supposed to become equal to the ground point due to the assumption of the point contact if the one-leg sliding state appears. On the other hand, in the case of asymmetric torque, the ZMP is away from the center of the support polygon at the start time and immediately converges because of the viscous friction of the motors. Moreover the ZMP dramatically approaches to the ground point just before takeoff, which shows that the state goes through the one-leg sliding where Leg 1 leaves the ground before Leg 2. Since the results are consistent with the behavior based on the analysis of the TSF, the validity of TSF is proved from the perspective of ZMP. In general, ZMP is determined despite the presence or absence of sliding whereas TSF explicitly includes sliding information. Therefore, with constraints between the coefficients of sliding friction and the centroid acceleration, TSF is effective for extraction and application of sliding information such as when the unknown coefficients of sliding friction can be calculated by using the slope of a line through the point of $\boldsymbol{g}$ in the centroid acceleration space because it corresponds to the boundary of the TSF. When the coefficients of sliding friction are known, the movable range of the centroid acceleration can be calculated in advance and be utilized to develop motion planning such that the acceleration is controlled not to move close to the vertex of the TSF to avoid takeoff. Note that these characteristics hold even when $\boldsymbol{\mu}_1 = \boldsymbol{\mu}_2$.

4. Legged Motion Based on Sliding Movement

In this section, the applications reflecting the analysis of sliding motion are considered. Focusing on the accelerated motion based on asymmetric friction and the conversion into the rotational motion

https://doi.org/10.1017/S0263574715000740 Published online by Cambridge University Press

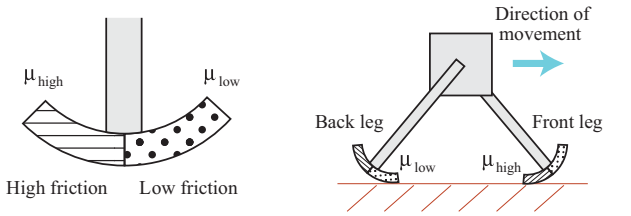

(a) Foot structure (b) Contact state with the ground

Fig. 11 Running strategy based on frictional asymmetry.

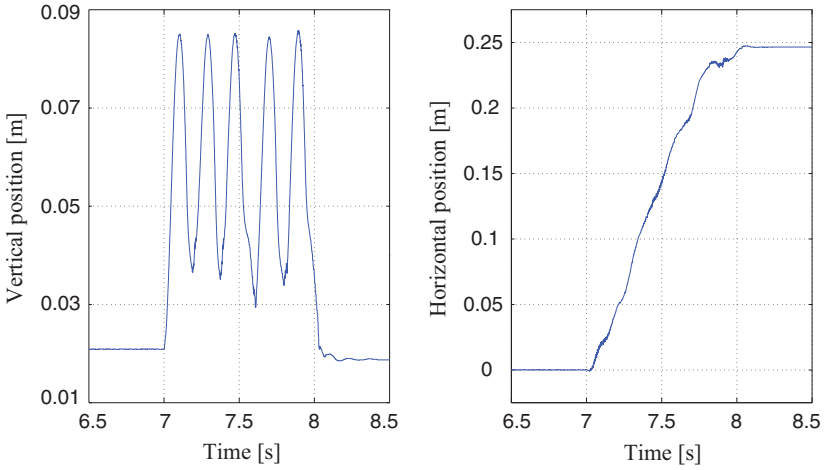

(a) Time response of vertical position (b) Time response of horizontal position

Fig. 12 Time response of centroid motion.

attributable to the asymmetric torque, running and somersaulting tasks are explained when these characteristics are applied.

4.1. Application to running[19]

4.1.1. Motion strategy. Consider running to be composed of the sliding motion of both legs in the inner direction and the jumping motion while switching the positions of both legs in the air. By setting asymmetric friction and symmetric torque expressed in Eq. (22) which results in accelerated motion, the goal of efficient running has an increase in the speed of sliding at the time of takeoff while conserving horizontal velocity in the air.

To generate a propulsive force in the same direction even if the front and back legs are counterchanged, we attach an asymmetric frictional material with curvature to each sole as shown in Fig. 11(a). This is composed of a low coefficient of friction μ_{low} in the front of the sole and a high coefficient of friction μ_{high} in the back of the sole along the x-axis. In this case, the frictional coefficient switches depending on the altitude of the robot as follows:

$$\mu_i = \begin{cases} \mu_{\text{high}} & \text{if } \theta_i > 0 \\ \mu_{\text{low}} & \text{if } \theta_i < 0 \end{cases}, \tag{24}$$

Accordingly, the contact state with high friction for the front leg and low friction for the back leg can be achieved as shown in Fig. 11(b). The asymmetric mechanism enables the robot to maintain continuous running motion in the positive direction of the x-axis.

https://doi.org/10.1017/S0263574715000740 Published online by Cambridge University Press

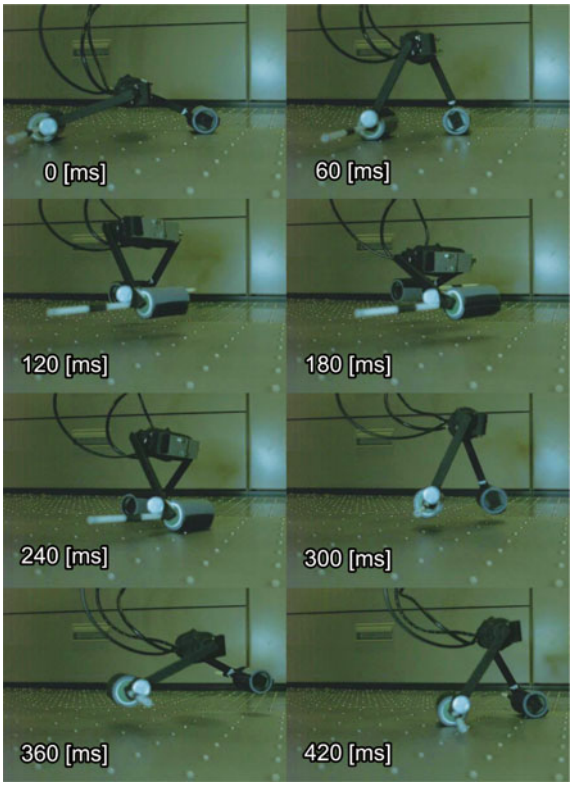

Fig. 13 Serial photographs of sliding and jumping motions.

4.1.2. Experiment. Set the input torque $\tau = \pm 0.9$ Nm and switch the sign to actuate the leg back and forth on each step. The coefficients of sliding friction are $\mu_{\text{high}} = 0.52$ and $\mu_{\text{low}} = 0.31$. At the moment of landing, which is measured with high-speed vision, the robot is controlled to start the next step for continuous running.

Figure 12(a) shows the time response of the vertical centroid position. It turns out that the robot achieves jumping because the vertical centroid position becomes higher than that in the upright posture 0.081 m. The average period of one step is 206 milliseconds which means that the robot can take 4.9 steps in one second. The jump height and the period on each step are maintained nearly constant which shows that stable running is achieved. Figure 12(b) shows the time response of the horizontal centroid position. This demonstrates the effect of the running strategy based on frictional asymmetry because continuous forward motion is observed. The horizontal movement with an average velocity of 0.24 m/s is achieved. Figure 13 shows a continuous sequence of pictures taken at intervals of 60 milliseconds. It shows that the robot runs while alternating the sliding motion and jumping motion repeatedly. These experimental results are shown as videos on the web site .[20]

4.2. Application to somersault

4.2.1. Motion strategy. Consider a somersault to be composed of one complete revolution with respect to the trunk angle, ignoring horizontal movement and landing posture to simplify the problem. By setting asymmetric torque and symmetric friction expressed by Eq. (23) that results in the conversion into rotational motion, the efficient somersault has an increase in angular momentum at the time of takeoff while conserving angular momentum in the air.

In the somersault task, it is important to increase the angular velocity of the trunk in the air and the vertical velocity at the time of takeoff because there are time constraints regarding flight duration and dynamic constraints expressed by Eqs. (10) and (11). Meanwhile, under the kinematic conditions of Eq. (13), the rotational motion of the trunk instantly stops as can be seen in Eq. (20) when the input torque of both legs are set to zero in the air. Therefore, set the connecting position of both legs at the distance of l_{g0} away from the trunk centroid so that the angular momentum acquired in the sliding

https://doi.org/10.1017/S0263574715000740 Published online by Cambridge University Press

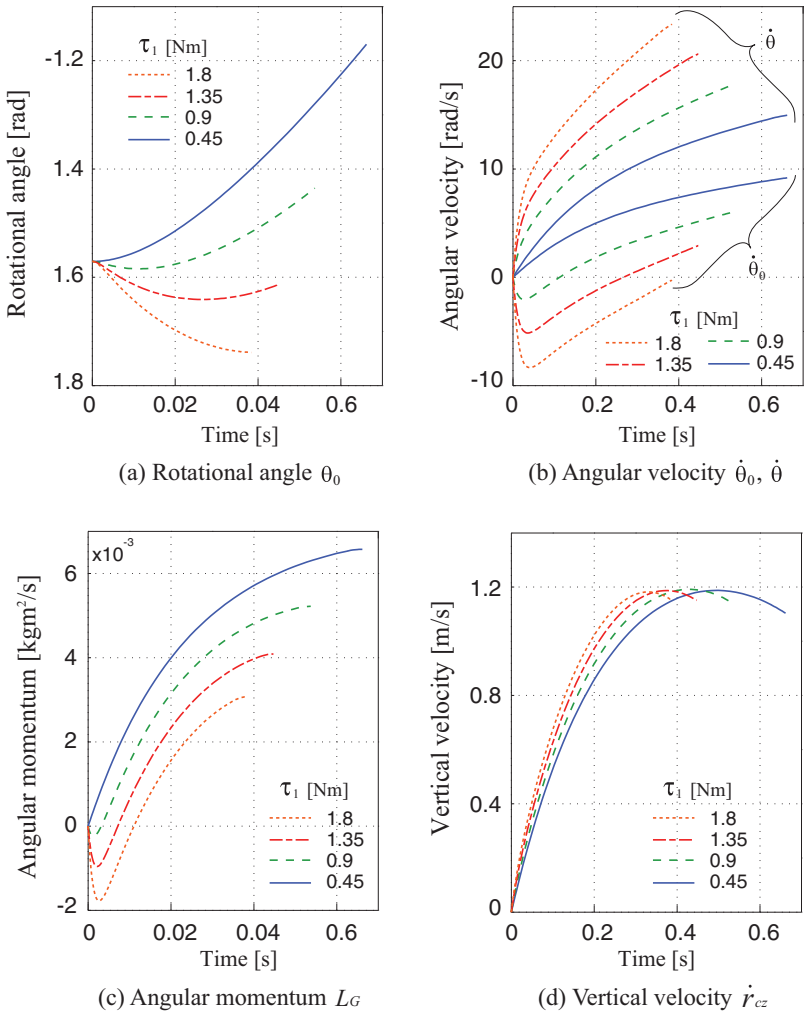

(a) Rotational angle θ_0 (b) Angular velocity $\dot{\theta}_0$, $\dot{\theta}$

(c) Angular momentum L_G (d) Vertical velocity $\dot{r}_{cz}$

Fig. 14 Sliding motion from the horizontal posture of the trunk.

motion is transformed into the angular velocity:

$$ {}^1\boldsymbol{r}_1 = {}^1\boldsymbol{r}_2 \neq \boldsymbol{r}_{c0}. \tag{25} $$

Then the effect of the torque asymmetry on the sliding motion until takeoff of both legs is shown in Fig. 14. It corresponds to varying the torque of τ_1 on the condition that $l_{g0} = 0.07$ m, $\tau_2 = -1.8$ Nm, and the initial posture of the trunk is horizontal at $\theta = -1.57$ radians. From Fig. 14(a), the larger the asymmetry of torque is, the larger is the rotational angle of the trunk as is the case with the analysis in Section 3. From Fig. 14(b) and (c), large asymmetry of the torque results in large angular momentum despite the decreasing angular velocity of the legs. On the other hand, there is little change in the vertical velocity of the centroid at the time of takeoff with changing the magnitude of the torque asymmetry from Fig. 14(d). This is because the decrease in the vertical velocity of legs is compensated by the increase in the vertical velocity of the trunk. Therefore, set the asymmetric torque to increase the angular momentum without slowing down the vertical velocity even in case of low input of energy as shown in Fig. 15(a).

After takeoff, both legs are controlled to parallel the long axis of the trunk due to the principle of conservation of angular momentum as shown in Fig. 15(b) thus minimizing the total moment of inertia for high-speed rotation of the trunk. At the time of takeoff, the motion is changed by setting the constant torque proportional to the angular difference between the trunk and each leg. After both

https://doi.org/10.1017/S0263574715000740 Published online by Cambridge University Press

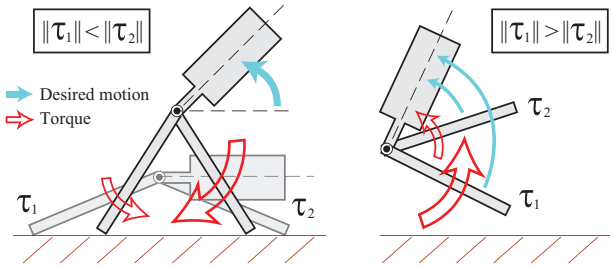

(a) Sliding phase (b) Jumping phase

Fig. 15 Somersault strategy based on torque asymmetry.

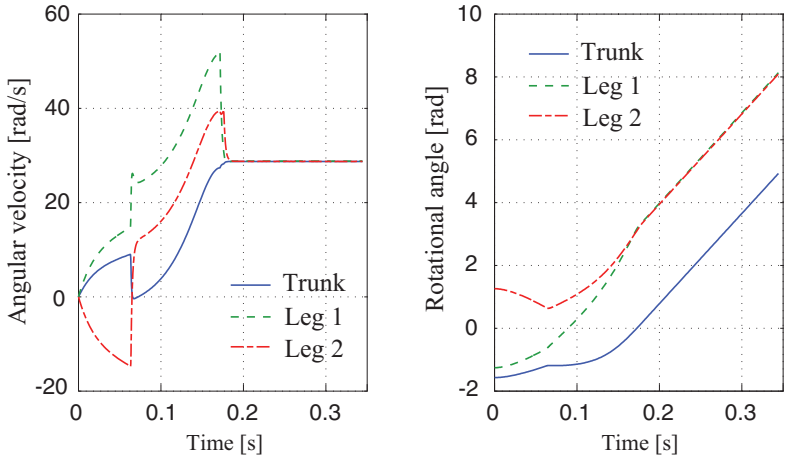

(a) Time response of angular velocity (b) Time response of rotational angle

Fig. 16 Simulation results of the somersault.

legs are parallel to the long axis of the trunk, the torques are set to zero to keep the angular velocity with a relatively fixed posture and to increase the total rotational angle of the trunk until the landing.

4.2.2. Numerical simulation. The input torques are set to $\tau_1 = 0.45$ Nm, $\tau_2 = -1.8$ Nm in the sliding motion and are normalized as $\tau_1 = 1.8$ Nm in the jumping phase.

Figure 16(a) shows the time response of the angular velocity. Until takeoff at $t = 0.063$ s, the angular velocity of the trunk increases during the sliding motion. Just after takeoff, it immediately decreases because of the rapid switching of the motion. However, it then instantly increases above the previous value due to the decrease in the total moment of inertia. It turns out that both legs are scissored to the trunk almost at the same time at around $t = 0.172$ s as can be seen from nearly simultaneous convergence of angular velocities of all links. After that, all angular velocities are constants due to the principle of conservation of angular momentum. Figure 16(b) shows the time response of the rotational angle. The initial posture of the trunk is horizontal as $\theta_0 = -1.57$ radians and dramatically increases in the air because of the large angular momentum acquired during the sliding motion. Finally the trunk angle is $\theta_0 = 4.92$ radians at the landing $t = 0.346$ s, and the total rotational angle reaches 6.49 radians, demonstrating the effect of the somersault strategy based on torque asymmetry. Figure 17 shows snapshots of the somersault animation taken at intervals of 43 milliseconds. The robot achieves the somersault which consists of one complete revolution of the trunk. These simulation results are shown as an animation on the web site .[21]

5. Conclusions

In this article, the state transition of a biped robot was formulated in centroid acceleration space based on sliding dynamics. The diagram was defined as a "triangle of sliding friction," and its characteristics were compared to a cone of friction. In addition, the concrete behavior of a 2-DOF model was analyzed

https://doi.org/10.1017/S0263574715000740 Published online by Cambridge University Press

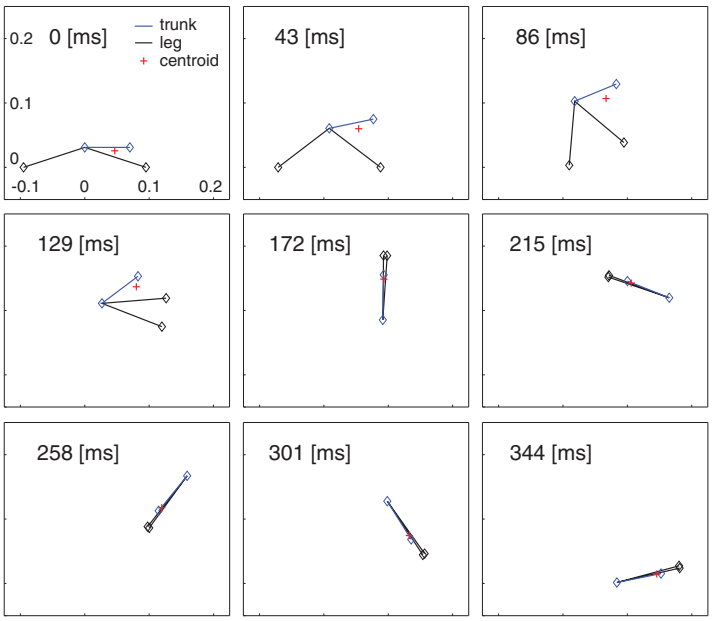

Fig. 17 Snapshots of the somersault.

with numerical simulation. It was found that asymmetry of sliding friction contributes not to rotational movement but to sliding acceleration whereas asymmetry of torque contributes to both elements where balance is determined by the viscous friction of the motors. Moreover, the sliding characteristics were applied to two tasks: running and somersaulting. The results demonstrate the validity of the proposed strategies based on the asymmetry of both friction and torque.

The obtained results are true under the limited condition of $\boldsymbol{\mu}_1 \neq \boldsymbol{\mu}_2$. Therefore, future work will concentrate on the improvement of TSF so that it includes the case of identical friction vectors. Three-dimensional TSF will be also investigated to include the case of applying a nonzero pushing force. Next, a trajectory planning and control method based on the analysis of TSF will be developed for achieving arbitrary sliding motion. They will be applied to concrete tasks such as the ski jump and the mogul. Moreover, a mixture model of sliding friction and static friction will be also considered with the goal of a seamless state transition between stationary and sliding.

Appendix

In this appendix, 3D sliding dynamics are added. Unlike the foregoing description, vectors are treated in 3D, and the cross-product is as generally defined. The x–y plane is set along the horizontal ground, and the z-axis is the vertical direction. When a unit vector, which represents sliding direction of each leg is $\boldsymbol{e}_{si}$, a friction vector is defined as follows:

$$\boldsymbol{\mu}_i \equiv -\mu_i \boldsymbol{e}_{si} + \begin{bmatrix} 0 & 0 & 1 \end{bmatrix}^T, \tag{26}$$

where $e_{siz} = 0$ is true because the sliding direction is represented on the x–y plane. In the 3D case, because a pushing force $\boldsymbol{F}_{pi}$ perpendicular to the sliding direction can be generated, the ground reaction force is expressed by the net force composed of sliding frictional force and pushing force:

$$\boldsymbol{N}_i \equiv N_{iz}\boldsymbol{\mu}_i + \boldsymbol{F}_{pi}. \tag{27}$$

By expressing the ground reaction force as in Eq. (27), the dynamics of Eq. (4) are true even in the 3D case.

Consider the case of $\boldsymbol{F}_{pi} = \boldsymbol{0}$. This corresponds to the case where 2D dynamics without a pushing force are extended to 3D dynamics. The following relation is derived by taking the cross product and

https://doi.org/10.1017/S0263574715000740 Published online by Cambridge University Press

the dot product of both sides of Eq. (4) with $\boldsymbol{\mu}_2$ and $\boldsymbol{\mu}_1$, respectively:

$$\left\{m_s(\ddot{\boldsymbol{r}}_c - \boldsymbol{g}) \times \boldsymbol{\mu}_2\right\} \cdot \boldsymbol{\mu}_1 = N_{1z}(\boldsymbol{\mu}_1 \times \boldsymbol{\mu}_2) \cdot \boldsymbol{\mu}_1 = 0. \tag{28}$$

By transforming the left-hand side using the formula of scalar triple product, the following constraint is obtained

$$(\ddot{\boldsymbol{r}}_c - \boldsymbol{g}) \cdot (\boldsymbol{\mu}_1 \times \boldsymbol{\mu}_2) = 0. \tag{29}$$

The constraint means the plane passes through the point of $\boldsymbol{g}$ and with normal vector $\boldsymbol{\mu}_1 \times \boldsymbol{\mu}_2$ in the acceleration space. That is, even in the 3D case, the movable range of the acceleration is constrained on a plane as in the 2D case.

Additionally, the normal force is calculated as

$$N_{1z} = \frac{m_s\left\{(\ddot{\boldsymbol{r}}_c - \boldsymbol{g}) \times \boldsymbol{\mu}_2\right\} \cdot (\boldsymbol{\mu}_1 \times \boldsymbol{\mu}_2)}{\|\boldsymbol{\mu}_1 \times \boldsymbol{\mu}_2\|^2}, \quad N_{2z} = \frac{m_s\left\{(\ddot{\boldsymbol{r}}_c - \boldsymbol{g}) \times \boldsymbol{\mu}_1\right\} \cdot (\boldsymbol{\mu}_2 \times \boldsymbol{\mu}_1)}{\|\boldsymbol{\mu}_1 \times \boldsymbol{\mu}_2\|^2}. \tag{30}$$

Because the normal force is always greater than zero, the movable range of acceleration is equivalent to the following area derived by transforming the Eq. (30)

$$(\ddot{\boldsymbol{r}}_c - \boldsymbol{g}) \cdot \left\{\boldsymbol{\mu}_2 \times (\boldsymbol{\mu}_1 \times \boldsymbol{\mu}_2)\right\} \geq 0, \quad (\ddot{\boldsymbol{r}}_c - \boldsymbol{g}) \cdot \left\{\boldsymbol{\mu}_1 \times (\boldsymbol{\mu}_2 \times \boldsymbol{\mu}_1)\right\} \geq 0. \tag{31}$$

Therefore, as in the 2D case, the boundaries of the common area between the plane (29) and the space (31) are expressed as follows:

$$(\ddot{\boldsymbol{r}}_c - \boldsymbol{g}) \times \boldsymbol{\mu}_2 = \boldsymbol{0}, \quad (\ddot{\boldsymbol{r}}_c - \boldsymbol{g}) \times \boldsymbol{\mu}_1 = \boldsymbol{0}. \tag{32}$$

As a result, a TSF can be represented as a triangle constrained to a 2D plane even in the 3D case.

References

1. T. Shibata, K. Sato, T. Takeshita, M. Iwase and S. Hatakeyama, "Study of Skating Robot," *Proceedings of the IEEE/ASME International Conference on Advanced Intelligent Mechatronics* (2008) pp. 1158–1163.
2. N. Ziv, Y. Lee and G. Ciaravella, "Inline Skating Motion Generator with Passive Wheels for Small Size Humanoid Robots," *Proceedings of the IEEE/ASME International Conference on Advanced Intelligent Mechatronics* (2010) pp. 1391–1395.
3. B. Nemec and L. Lahajnar, "Control and Navigation of the Skiing Robot," *Proceedings of the IEEE/RSJ International Conference on Intelligent Robots and Systems* (2009) pp. 2321–2326.
4. L. Lahajnar, A. Kos and B. Nemec, "Skiing robot - design, control, and navigation in unstructured environment," *Robotica* **27**(4), 567–577 (2009).
5. T. Petric, A. Gams, J. Babic and L. Zlajpah, "Reflexive stability control framework for humanoid robots," *Auton. Robots* **34**(4), 347–361 (2013).
6. K. Miura, F. Kanehiro, K. Harada, S. Kajita and K. Yokoi, "Slip-turn for biped robots," *IEEE Trans. Robot.* **29**(4), 875–887 (2013).
7. K. Hashimoto, Y. Yoshimura, H. Kondo, H. Lim and A. Takanishi, "Realization of Quick Turn of Biped Humanoid Robot by Using Slipping Motion with Both Feet," *Proceedings of the IEEE International Conference on Robotics and Automation* (2011) pp. 2041–2046.
8. M. Koeda, Y. Uda, S. Sugiyama and T. Yoshikawa, "Shuffle Turn and Translation of Humanoid Robots," *Proceedings of the IEEE International Conference on Robotics and Automation* (2011) pp. 593–598.
9. J. S. Yeon and J. H. Park, "A fast turning method for biped robots with foot slip during single-support phase," *IEEE/ASME Trans. Mechatronics* **19**(6), 1847–1858 (2014).
10. K. Kaneko, F. Kanehiro, S. Kajita, M. Morisawa, K. Fujiwara, K. Harada and H. Hirukawa, "Slip Observer for Walking on a Low Friction Floor," *Proceedings of the IEEE/RSJ International Conference on Intelligent Robots and Systems* (2005) pp. 634–640.
11. M. Higashimori, M. Harada, M. Yuya, I. Ishii and M. Kaneko, "Dimensional Analysis Based Design on Tracing Type Legged Robots," *Proceedings of the IEEE International Conference on Robotics and Automation* (2005) pp. 181–187.
12. M. Mori and S. Hirose, "Locomotion of 3D Snake-like robots – shifting and rolling control of active cord mechanism ACM-R3–," *J. Robot. Mechatronics* **18**(5), 521–528 (2006).
13. A. A. Transeth, R. I. Leine, C. Glocker and K. Y. Pettersen, "3-D snake robot motion: Nonsmooth modeling, simulations, and experiments," *IEEE Trans. Robot.* **24**(2), 361–376 (2008).

https://doi.org/10.1017/S0263574715000740 Published online by Cambridge University Press

14. B. Gamus and Y. Or, "Analysis of Dynamic Bipedal Robot Walking with Stick-Slip Transitions," *Proceedings of the IEEE International Conference on Robotics and Automation* (2013) pp. 3348–3355.
15. A. Tavakoli and Y. Hurmuzlu, "Robotic locomotion of three generations of a family tree of dynamical systems – Part I: Passive gait patterns–," *Nonlinear Dyn.* **73**(3), 1969–1989 (2013).
16. T. Senoo and M. Ishikawa, "Two-Dimensional Analysis of Dynamic Biped Locomotion Based on Feet Slip," *Proceedings of the IEEE/ASME International Conference on Advanced Intelligent Mechatronics* (2013) pp. 512–517.
17. G. J. Ingen Schenau and K. Bakker, "A biomechanical model of speed skating," *J. Human Mov. Stud.* **6**, 1–18 (1980).
18. A. Hache, *The Physics of Hockey* (2715 North Charles Street, Baltimore, Maryland 21218-4363, Johns Hopkins University Press, 2003) pp. 41–48.
19. T. Senoo, M. Takano and M. Ishikawa, "Dynamic Horizontal Movement of a Bipedal Robot Using Frictional Asymmetry," *Proceedings of the IEEE/RSJ International Conference on Intelligent Robots and Systems* (2012) pp. 1834–1839.
20. Ishikawa Watanabe Laboratory, "Slip running using frictional asymmetry," Accessed on 24 April 2015, http://www.k2.t.u-tokyo.ac.jp/fusion/AsymmetricFriction/
21. Ishikawa Watanabe Laboratory, "Sliding somersault using torque asymmetry," Accessed on 24 April 2015, http://www.k2.t.u-tokyo.ac.jp/fusion/SlidingSomersault/

https://doi.org/10.1017/S0263574715000740 Published online by Cambridge University Press